Internal triaxial strain imaging of visibly opaque black rubbers with terahertz polarization spectroscopy

Atsuto Moriwaki[a)], Makoto Okano[a)], and Shinichi Watanabe

Department of Physics, Faculty of Science and Technology, Keio University, 3-14-1 Hiyoshi, Kohoku-ku, Yokohama, Kanagawa 223-8522, Japan

Abstract

We demonstrate the nondestructive imaging of internal triaxial strain in visibly opaque black rubbers by employing the polarization-sensitive terahertz time-domain spectroscopy (PS THz-TDS) technique. From the sample thickness and the differences in amplitude and phase between orthogonal components of the terahertz wave that passed through the sample, the degree of birefringence and the angle of the slow optic axis were determined. We were able to convert the birefringence data into the amount and orientation of the internal strain through a Monte Carlo simulation that correlates the birefringent properties of the rubber with the deformation. By comparing the strain map obtained from the PS THz-TDS measurements with that obtained by conventional digital image correlation, we found that both experimental spatial distributions of the strain are in overall good agreement, except around the clamped sample regions. The deviations results from the intrinsic difference in the obtained strain information between two experiments and it is confirmed that our method based on the PS THz-TDS is suited for evaluating the spatial distribution of the internal strain in black rubbers.

a) A. Moriwaki and M. Okano contributed equally to this work.

During the past century, polymeric materials have emerged as one of the most popular and useful materials because of their abundant convenient features, such as mass productivity, light weight, and low cost. These advantages allow extensive use in various electrical, industrial, and medical products.[1] From the viewpoints of product life and environmental aspects, it is essential to evaluate the defects in the polymeric materials. In particular, because it is well known that the strain localization leads to failure through cracks,[2,3] the evaluation of the spatial strain distribution is quite important. To date, numerous techniques have been introduced for evaluating the strain, for example by using X-ray,[4,5] visible light,[6] and electric[7] and optical strain gauging.[8] The strain evaluation techniques based on visible light such as the photoelasticity[9,10] and digital image correlation (DIC) techniques[11,12] have a clear advantage compared with other methods. Using visible light, one can achieve a non-contact, *in-situ*, and nondestructive evaluation of the materials, because the visible light requires no waveguide in the vicinity of the sample and inflicts less damage on the sample compared with X-ray. However, visible light cannot access the internal strain in visibly opaque materials, although most polymer-based practical products are opaque for visible light. Hence, the development of an evaluation method for the internal strain in optically opaque materials is urgently required.

Terahertz spectroscopy is an emerging and powerful optical technique for nondestructive evaluation of visibly opaque materials.[13–25] Since terahertz waves have relatively low photon energies (~meV), they can penetrate the visibly opaque materials without damage. Among the visibly opaque materials, the black rubbers, such as styrene-butadiene rubbers and fluoroelastomers, are one of the most important materials for our modern civilization, because they are widely used in tires, vibration absorbers, and also as sealing materials. It is known that conductive carbon fillers that are embedded in black rubbers have a large impact on the optical responses of the black rubbers in the terahertz

frequency region.[14–19,22–24] Moreover, very recently, we found that the conductive carbon black aggregates embedded in fluoroelastomer show a large optical anisotropy that is governed by the alignment of the anisotropically shaped carbon black aggregates.[24] It is interesting that this optical anisotropy can be strongly modulated by deformation of the fluoroelastomer–carbon-black composites. This experimental result suggests that the strain in the black rubbers can be probed through the change in the optical anisotropy. An experimental demonstration of the nondestructive evaluation of the internal strain in black rubbers by means of terahertz spectroscopy would be highly valuable for further research activities on advanced terahertz applications.

In this work, we report a method for evaluating the internal strain in a visibly opaque styrene-butadiene rubber with polarization-sensitive terahertz time-domain spectroscopy (PS THz-TDS). In order to determine the internal strain, we initially measured the spatial image of the birefringent properties and the thickness of the sample. By comparing the measured birefringence with the Monte Carlo (MC) simulation results that correlate birefringence and strain, we obtained the triaxial strain image of the sample under loaded conditions. In order to confirm the validity of our evaluation method, we compared the obtained strain image with that obtained by the conventional DIC analysis. It is found that both strain images match well at the center area of the sample, where the sample is without any constraints. The deviations of both data sets in the clamped sample regions reflect the intrinsic difference in the obtained information between two experiments. We concluded that our evaluation method using terahertz waves is suited for a non-contact analysis of opaque black rubbers without edge constraints.

The sample in this work was a rectangular styrene-butadiene rubber sheet containing 15

wt% carbon-black fillers and had extensions of 1 x 20 x 50 mm^3 corresponding to thickness (z-axis), short axis (y-axis), and long axis (x-axis), respectively. In order to perform the DIC analysis, we sprayed a white rubber ink on the surface of the rectangular sample prior to the imaging experiment (see inset of Fig. 1). We confirmed that the sprayed ink had no impact on the PS THz-TDS experiment. The PS THz-TDS was performed using a commercially available high-speed THz-TDS system (T-ray 5000, Advanced Photonix. Inc.) in combination with a rotating wire-grid polarizer.[24,26,27] The schematic view of the experimental setup is shown in Fig. 1. The photoconductive antennas were used for the terahertz transmitter and receiver. We placed a half-wave plate that is optimized at 0.6 THz in front of the terahertz transmitter, to vary the polarization states of light at different frequencies. The frequency-dependent polarization is essential to determine the birefringent properties of the sample as described in the previous study.[24] The beam spot of the terahertz pulse was measured carefully by the knife-edge method, and was estimated to be 2–3 mm at 0.2–0.4 THz. In our terahertz method, we measured the polarization of the terahertz pulse with and without the sample, and then we obtained the angle of the slow optic axis ($\theta(\omega)$) of the sample with regard to the x-axis and the phase retardation ($\Delta(\omega)$) between the two optic axes The details of the experimental setup and numerical analysis to determine $\theta(\omega)$ and $\Delta(\omega)$ are described elsewhere.[24] In the PS THz-TDS, both the thickness of the sample (t) and the refractive indices along the two optic axes were evaluated by using a modified total variation

metric,[28] which measures the smoothness of the complex refractive-index functions along the two optic axes to identify which thickness and complex refractive index pair are more appropriate for the measured sample.[28] After calculating the degree of birefringence ($\Delta n(\omega)$) by using the following relation, $\Delta n(\omega) = \frac{\Delta(\omega)c}{t\omega}$, where c is the speed of light, we averaged the θ and Δn over the frequency range 0.2–0.4 THz. The experimental error in Δn was estimated to be below 0.002 in our experimental system.

The terahertz strain imaging experiments were conducted as follows. First, we clamped both short edges of the sample with aluminum blocks on appropriate two-axes computer-controlled translation stages, which can move in x- and y-directions and are used to set a certain draw ratio (DR) of the sample. Here, we label the directions parallel and perpendicular to the stretching direction with x and y, respectively. The DR is defined with DR = L/L_0 where L and L_0 are the final and initial lengths along the stretching direction (x-axis). With regard to the image data, we repeated the terahertz and DIC measurements while the DR was successively changed between 1 (unloaded) and 2.1 in seven steps. The measurement sequence started with the PS THz-TDS imaging. The map data was taken with a resolution of 1 mm, and to record one complete image typically 10–15 min were required. After the image measurement with the PS THz-TDS, the sample was moved to the image acquisition position for the DIC analysis with a complementary metal–oxide–semiconductor camera. We took one image of the sample surface for each DR, which was controlled by the translation stages. After recording the photograph, the sample was moved back to the PS THz-TDS imaging part of the setup. A waiting period of 30 s was included to avoid any effect of the initial fast stress relaxation on the birefringence measurement after setting the next DR. Then, we again performed the next imaging sequence starting with the PS THz-TDS imaging

experiment. Because the spot size of the terahertz beam in our system was about 3 mm, the experimental data near the edges of the sample necessarily include some experimental error. In this work, we show the experimental data excluding that obtained close to the edges. For the DIC analysis, we used the open source software Ncorr to obtain the spatial mapping of the surface strain.[29] All measurements were performed at room temperature.

Figures 2(a)–(d) show the spatial mappings of Δn and θ of the sample for DR = 1 and 1.36. According to the beam spot size of the terahertz pulse, the spatial resolution was estimated to be 3 mm, corresponding to 3 pixels in Fig. 2. In addition, because the measurement around the edges of the sample has to contain the unavoidable experimental error due to the scattering from the sample edges, we only show and discuss the experimental results at the positions of 3 mm far from the sample edges, where the experimental error is small. As shown in Fig. 2(a), the Δn under the unloaded condition is less than 0.03 over the whole area except for the right and left edge regions. Since the large Δn at the edges might be due to extrinsic effects or an experimental error, we conclude that the actual Δn is small everywhere in the sample. On the contrary, Fig. 2(b) shows that θ exhibits a strong fluctuation. It has been reported that Δn and θ are determined by the degree of orientation and the averaged orientation angle of the carbon black aggregates, respectively.[24] Thus, these results indicate that the carbon black aggregates in the sample are almost randomly oriented for DR = 1. As shown in Figs. 2(c) and (d), by changing DR to 1.36, Δn becomes larger everywhere and θ converges to 0. Therefore, we consider that the DR-dependence of the birefringent properties can be well explained by the orientation of the anisotropically shaped carbon black aggregates along the stretching direction.[24] It is found that for DR = 1.36, the Δn at the center of the sample is larger than that near the right and left edges. Because the edge regions of the sample are fixed by a clamp, the small Δn at the edges indicates that a constrained deformation affects Δn.

Let us now explain the procedure to derive the spatial distribution of the internal triaxial strain in the sample. First, we assumed that one of the three principal axes of the strain tensor is parallel to the *z*-axis, which corresponds to the propagation direction of the terahertz wave and the thickness direction of the sample. Thus, the strain tensor $\hat{\epsilon}$ in the Cartesian coordinate system with *x*-, *y*-, and *z*-axes is described as follows;

$$\hat{\epsilon} = \begin{pmatrix} \varepsilon_{xx} & \varepsilon_{xy} & 0 \\ \varepsilon_{xy} & \varepsilon_{yy} & 0 \\ 0 & 0 & \varepsilon_{zz} \end{pmatrix}. \quad (1)$$

Here, the first subscript denotes the surface normal direction and the second subscript the direction of the strain. After an optimal transformation of the coordinate system, we can obtain the diagonalized principal strain tensor $\widehat{\epsilon'}$,

$$\widehat{\epsilon'} = \begin{pmatrix} \varepsilon_1 & 0 & 0 \\ 0 & \varepsilon_2 & 0 \\ 0 & 0 & \varepsilon_3 \end{pmatrix}, \quad (2)$$

where ε_1, ε_2, and ε_3 are the three principal strains. The relationship between $\widehat{\epsilon'}$ and $\hat{\epsilon}$ is written as;

$$\hat{\epsilon} \equiv \begin{pmatrix} \cos\theta' & -\sin\theta' & 0 \\ \sin\theta' & \cos\theta' & 0 \\ 0 & 0 & 1 \end{pmatrix} \cdot \widehat{\epsilon'} \cdot \begin{pmatrix} \cos\theta' & \sin\theta' & 0 \\ -\sin\theta' & \cos\theta' & 0 \\ 0 & 0 & 1 \end{pmatrix}, \quad (3)$$

where θ' represents the angle between the *x*-axis and the principal axis for ε_1. Using Eq. (3) we determined the parameters ε_{xx}, ε_{xy}, ε_{yy}, and ε_{zz} in Eq. (1) from the experimentally-determined parameters ε_1, ε_2, ε_3, and θ' at each position (x, y) obtained *via* the PS THz-TDS.

Next, we explain the procedure for determining the parameters ε_1, ε_2, ε_3, and θ' from the experimentally obtained birefringence properties. The procedure relies on a numerical calculation of the relationship between the birefringent properties and strain. Here,

we assumed uniaxial ellipsoids for the anisotropically shaped carbon black aggregates and a constant volume deformation.[24] In addition, we considered that the ellipsoidal carbon black aggregates in the unloaded samples are randomly oriented, which is supported by the experimental results (see Figs. 2 (a) and (b)). In this case, θ' is identical with the θ determined by the PS THz-TDS measurement, since the averaged orientation direction is parallel to the strain direction. The choice of the coordinate system also allows to express ε_3 with the thickness ratio of the sample before (t_0) and after (t) the stretching measured by the THz-TDS experiment; $\varepsilon_3 = (t - t_0)/t_0$. Finally, we determined ε_1 and ε_2 from ε_3 and Δn by assuming constant-volume deformation. The latter assumption is expressed by the following equation;

$$(\varepsilon_1 + 1) \cdot (\varepsilon_2 + 1) \cdot (\varepsilon_3 + 1) = 1. \quad (4)$$

By introducing a parameter α, which describes the ratio of deformation along the directions parallel and perpendicular to the stretched direction, we can define $\varepsilon_1 = (\varepsilon_3 + 1)^{-\alpha} - 1$ and $\varepsilon_2 = (\varepsilon_3 + 1)^{(\alpha-1)} - 1$. By choosing an appropriate α, we can explain various deformation processes with the constraints mentioned above.

As outlined in the previous paragraph, the conversion of the birefringent properties to strain requires the knowledge of the parameter α at each position. To determine α, we assumed that the biaxial orientation distribution in the *x*-*y* plane determines Δn in our samples. In this case, Δn is expressed by[30]

$$\Delta n = (f_x - f_y)\Delta n_0 \quad (5)$$

where Δn_0 is the intrinsic birefringence, i.e., the birefringence in the case when perfect alignment is achieved, and f_x and f_y are the biaxial orientation factors of an ensemble of carbon black aggregates for *x*- and *y*-directions, respectively. These factors are described as follows

$$f_x = 2\langle \cos^2 \phi_x \rangle + \langle \cos^2 \phi_y \rangle - 1, \quad (6)$$

$$f_y = 2\langle \cos^2 \phi_y \rangle + \langle \cos^2 \phi_x \rangle - 1, \quad (7)$$

where the $\langle \cdots \rangle$ represents the ensemble average and ϕ_x and ϕ_y are angles between the major axis of each carbon black aggregate and the *x*- and *y*-axes, respectively. When the sample is stretched, the angle of each ellipsoidal carbon black aggregate is changed because they tilt towards the stretching direction, which causes a change in $f_x - f_y$. Since the stretching deformation strongly depends on α, the ε_3-dependence of $f_x - f_y$, i.e., Δn (Eq. (5)), is also sensitive to α. In order to find the appropriate α, we first calculated the relationship between α and $f_x - f_y$ by a MC simulation according to our previous study,[24] and then we compared the calculated Δn derived from $f_x - f_y$ by Eq. 4 with the experimental results.

The solid curve in Fig. 3 shows the theoretical ε_3-dependence for Δn with α = 2 and Δn_0 = 0.47. Since our previous study revealed that the Poisson's ratio in the rubber materials is approximately 0.5 (corresponding to $\alpha = 2$) at the center position of the sample, the value of Δn_0 can be estimated from the experimentally obtained ε_3-dependence of Δn at the center position of the sample. As shown in Fig. 2, our simple simulation model can reproduce the ε_3-dependence of Δn at the center. We determined the appropriate values of α for all positions on the sample by comparing the measured image data of Δn and ε_3 with the numerical results for various values of α. After estimating the spatial mapping of the parameter α, we calculated the components of the strain tensor by using Eqs. (2)-(4).

Figures 4(a)–(d) show the images of ε_{zz}, ε_{xx}, ε_{yy}, and ε_{xy} estimated from the PS THz-TDS experiments for DR = 1.36. The characteristic features in the spatial distribution of all strain components are explained in the following. First, except in the edges of the sample, the value of ε_{xx} is almost the same as the numerical value of 0.36 (DR-1), verifying the

validity of our method. Second, we found that $|\varepsilon_{zz}|$ is larger than $|\varepsilon_{yy}|$ near the right and left edges. This is a result of the clamp that prevents the shrinkage of the sample along the y-direction, resulting in a stronger compression in z-direction. Third, $|\varepsilon_{zz}|$ and $|\varepsilon_{yy}|$ are almost the same at the center, which means that the volume elements without any constraints have a Poisson's ratio of 0.5 (i.e., the styrene-butadiene rubber sample behaves as an almost ideal elastic material). Finally, all images show a slightly asymmetric pattern that most likely results from slightly different mounting conditions at the right and left edges of the sample. We emphasize that the advantage of our method is that it is able to evaluate the triaxial strain images based on the changes in the thickness and the birefringent properties at each spatial position alone, without any need of preprocessing.

In order to understand the accuracy of our evaluation method, we compared the ε_{xx} and ε_{yy} images determined from PS THz-TDS (Figs. 4(b) and (c)) with those obtained by the two-dimensional (2D) DIC analysis. We stress that the former method investigates the triaxial internal strain of the sample, while the latter method investigates the 2D surface strain.[11] Although the obtained information in the two methods might be different, a comparison between the two methods is helpful to shed light on the limitations of the present analysis method and its potential applications.

Figures 5(a) and (b) show the spatial mappings of the surface strain ε_{xx} and ε_{yy} estimated from the DIC analysis for DR = 1.36. At the center of the sample, the strain maps obtained from PS THz-TDS and DIC show a similar spatial distribution. Figures 5(c) and (d) show the DR dependence of ε_{xx} (Fig. 5(c)) and ε_{yy} (Fig. 5(d)) at y = 0 as determined by DIC and PS THz-TDS with the solid curves and filled circles, respectively. The results of the two methods are in good agreement around the center position of the sample. This agreement evidences that our method is useful for estimation of the strain distribution of rubber samples

in a contactless manner. We note that around the edges of the sample, a large discrepancy between the data obtained by the PS THz-TDS and the DIC analysis is observed. Because the PS THz-TDS and the DIC analysis obtain the internal and surface strain, respectively, this discrepancy would reflect the intrinsic difference between two methods. However, at present, because we cannot assess the other effects, such as the failure of the constant-volume approximation, on the discrepancy in the strain distribution, further investigations are deserved.

Finally, we briefly mention the benefit and potential application of our strain evaluation method using the PS THz-TDS. As mentioned above, our evaluation method can probe the internal strain of the rubber samples, which cannot be assessed by the conventional optical techniques with visible light, without any damages and any preprocesses. Since the inspection of the internal strain of the rubber materials prevents the failure of the instruments and machines partially consisting of the rubber parts, our method is useful in terms of the safety and cost saving. Moreover, it is considered that our evaluation method is expanded for other materials straightforwardly. Since the most essential point of our evaluation method is that one converts the birefringent properties into the strain based on the relationship between the birefringent properties and the strain. Therefore, if we know or calculate the relationship between them for other materials, such as polymeric materials, we can determine the strain from the measured birefringent properties in other materials as well as rubber materials. Thus, our terahertz method has clear advantages such as non-contact and nondestructive inspection without need of any preprocessing such as surface patterning and large potential applications.

In summary, we demonstrated a nondestructive evaluation method for internal triaxial strain in the styrene-butadiene rubber samples. This method measures the birefringent properties of the stretched samples with PS THz-TDS, and by using the relationship between

the birefringence and strain, which was obtained from a MC simulation, we were able to evaluate the triaxial strain in the sample. In order to understand the accuracy of our evaluation method, we also performed the conventional DIC surface strain measurement and compared the results with those obtained by the PS THz-TDS measurements. Both data sets are almost the same in the center region of the sample, while deviations were found around the clamped edges of the samples. The deviation results from the intrinsic difference between the PS THz-TDS and the DIC measurements. It is concluded that our evaluation method using the terahertz spectroscopy is a powerful tool suited for visibly opaque black rubbers, potentially useful for industrial applications and research activities on advanced terahertz applications.

Acknowledgements

This work was partially supported by Japan Science and Technology Agency (JST) under Collaborative Research Based on Industrial Demand "Terahertz-wave: Towards Innovative Development of Terahertz-wave Technologies and Applications", and a Grant-in-Aid from the Ministry of Education, Culture, Sports, Science, and Technology, Japan for the Photon Frontier Network Program.

References

1. D. V. Rosato, *Plastics End Use Applications* (Springer, 2011).
2. F. Armero and K. Garikipati, Int. J. Solids Structures, **33**, 2863 (1996).
3. X. Sun, K. S. Choi, W. N. Liu, and M. A. Khaleel, Int. J. Plastics, **25**, 1888 (2009).
4. S. S. Russell and M. A. Sutton, Exp. Mech. **29**, 237 (1989).
5. B. K. Bay, T. S. Smith, D. P. Fyhrie, and M. Saad, Exp. Mech. **39**, 217 (1999).
6. J. E. Field, S. M. Walley, W. G. Proud, H. T. Goldrein, and C. R. Siviour, Int. J. Impact. Eng. **30**, 725 (2004) and reference there in.
7. J. Herrmann, K.-H. Müller, T. Reda, G. R. Baxter, B. Raguse, G. J. J. B. de Groot, R. Chai, M. Roberts, and L. Wieczorek, Appl. Phys. Lett. **91**, 183105 (2007).
8. C. D. Butter and G. B. Hocker, Appl. Opt. **17**, 2867 (1978).
9. L. R. G. Treloar, Trans. Faraday Soc. **43**, 284 (1947).
10. T. Capelle, Y. Tsaturyan, A. Barg, and A. Schliesser, Appl. Phys. Lett. **110**, 181106 (2017);
11. T. C. Chu, W. F. Ranson, M. A. Sutton and W. H. Peters, Exp. Mech. **25**, 232 (1985).
12. M. H. Malakooti1 and H. A. Sodano, Appl. Phys. Lett. **102**, 061901 (2013).
13. F. Rutz, T. Hasek, M. Koch, H. Richter, and U. Ewert, Appl. Phys. Lett. **89**, 221911 (2006).
14. S. Wietzke, C. Jansen, F. Rutz, D.M. Mittleman, and M. Koch, Polym. Test. **26**, 614 (2007).
15. R. Rungsawang, V. G. Geethamma, E. P. J. Parrott, D. A. Ritchie, and E. M. Terentjev, J. Appl. Phys. **103**, 123503 (2008).
16. Y. Ji, Y. Y. Huang, R. Rungsawang, and E. M. Terentjev, Adv. Mater. **22**, 3436 (2010).
17. Y. Hirakawa, Y. Ohno, T. Gondoh, T. Mori, K. Takeya, M. Tonouchi, H. Ohtake, and T. Hirosumi, J. Infrared. Milli. Terahz. Waves **32**, 1457 (2011).
18. J. Macutkevic, D. Seliuta, G. Valusis, R. Adomavicius, P. Kuzhir, A. Paddubskaya, M.

Shuba, S. Maksimenko, L. Coderoni, F. Micciulla, I. Sacco, and S. Bellucci, Chem. Phys. **404**, 129 (2012).

19. O. Peters, S. F. Busch, B. M. Fischer, and M. Koch, J. Infrared. Milli. Terahz. Waves **33**, 1221 (2012).
20. S. Katletz, M. Pfleger, H. Pühringer, M. Mikulics, N. Vieweg, O. Peters, B. Scherger, M. Scheller, M. Koch, and K. Wiesauer, Opt. Express **20**, 23025 (2012).
21. M. Pfleger, H. Pühringer, and S. Katletz, Proceedings of 39th International Conference on Infrared, Millimeter, and Terahertz waves (IRMMW-THz) (2014).
22. R. Casini, G. Papari, A. Andreone, D. Marrazzo, A. Patti, and P. Russo, Opt. Express **23**, 18181 (2015).
23. E. V. Yakovlev, K. I. Zaytsev, I. N. Dolganova, and S. O. Yurchenko, IEEE Trans. THz Sci. Technol. **5**, 810 (2015).
24. M. Okano and S. Watanabe, Sci. Rep. **6**, 39079 (2016).
25. H. Iwasaki, M. Nakamura, N. Komatsubara, M. Okano, M. Nakasako, H. Sato, and S. Watanabe, J. Phys. Chem. B. (doi: 10.1021/acs.jpcb.7b04755)
26. C. M. Morris, R. Valdes Aguilar, A. V. Stier, and N. P. Armitage, Opt. Express 20, 12303 (2012).
27. J.-B. Masson and G. Gallot, Opt. Lett. **31**, 265 (2006).
28. T. D. Dorney, R. G. Baraniuk, D. M. Mittleman, J. Opt. Soc. Am. A **18**, 1562 (2001).
29. J. Blaber, B. Adair, and A. Antoniou, Exp. Mech. **55**, 1105 (2015).
30. J. L. White and J. E. Spruiell, Poly. Eng. Sci. **21**, 859 (1981).

List of Figure legends

FIG. 1: Schematic view of the experimental setup. Inset: Photograph of the sprayed rubber sample.

FIG. 2: Spatial mapping of the degree of birefringence Δn ((a) and (c)) and angle θ of optic axis with respect to the x-direction ((b) and (d)) for the sample with DR = 1 and 1.36 in the left- and right-hand side figures, respectively. The measured values were averaged over the frequency range 0.2–0.4 THz

FIG. 3: ε_3-dependence of the degree of birefringence of the sample at the center position of the sample. The symbols correspond to the experimental data. The solid curve represents the data calculated with $\alpha = 2$ and $\Delta n_0 = 0.47$.

FIG. 4: Triaxial strain images of the sample for DR = 1.36 obtained from the PS THz-TDS data. (a) ε_{zz} evaluated from the ratio of thicknesses after and before deformation. (b) ε_{xx}, (c) ε_{yy}, and (d) ε_{xy} drived from the spatial distribution of the birefringent properties.

FIG. 5: Spatial distribution of (a) ε_{xx} and (b) ε_{yy} evaluated by the DIC analysis. Line profiles of (c) ε_{xx} and (d) ε_{yy} at $y = 0$ for various DRs. Symbols and solid curves correspond to the data evaluated from the PS THz-TDS and DIC analysis, respectively. Red, yellow, green, spring green, cyan, and blue data correspond to strain for DRs of 1.18, 1.36, 1.54, 1.72, 1.89, and 2.08, respectively.

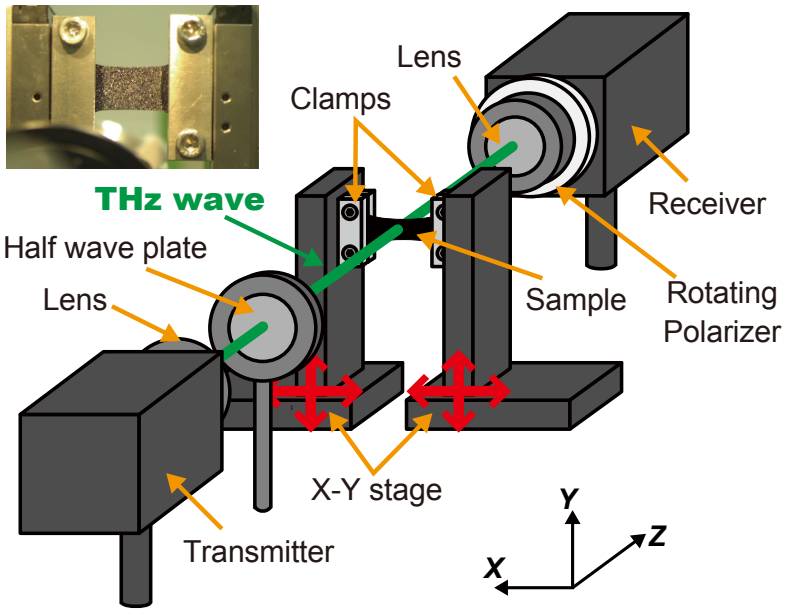

Figure 1.

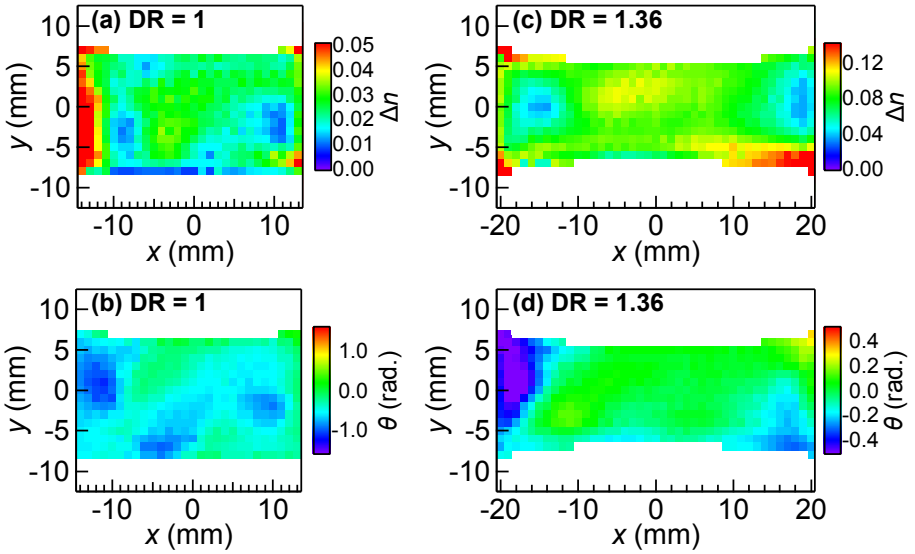

Figure 2.

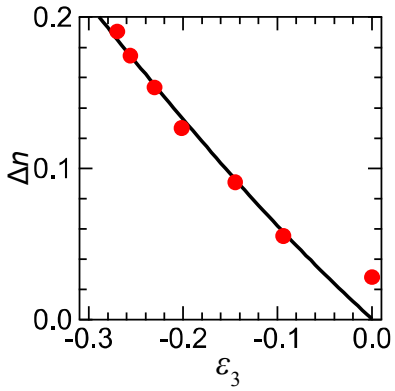

Figure 3.

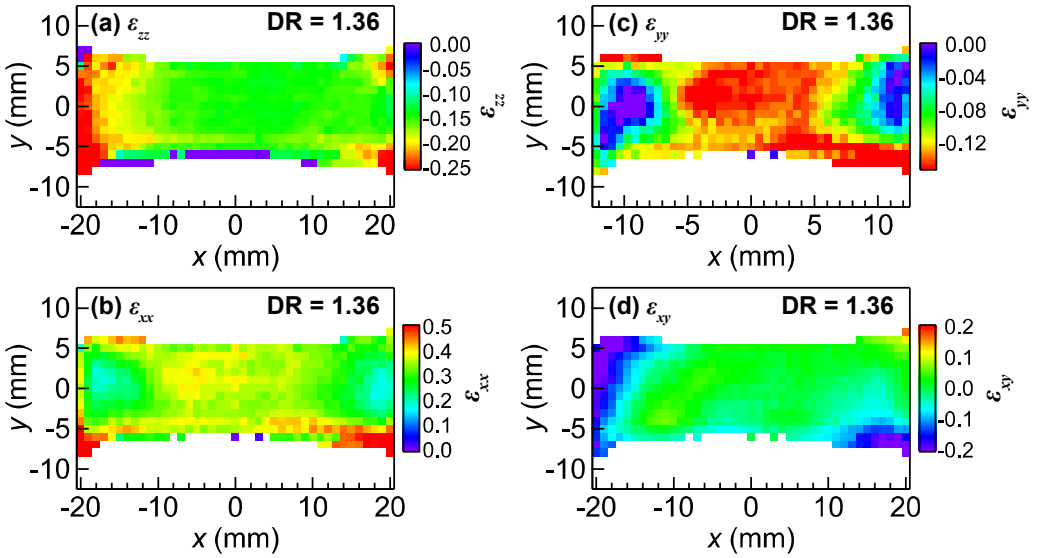

Figure 4.

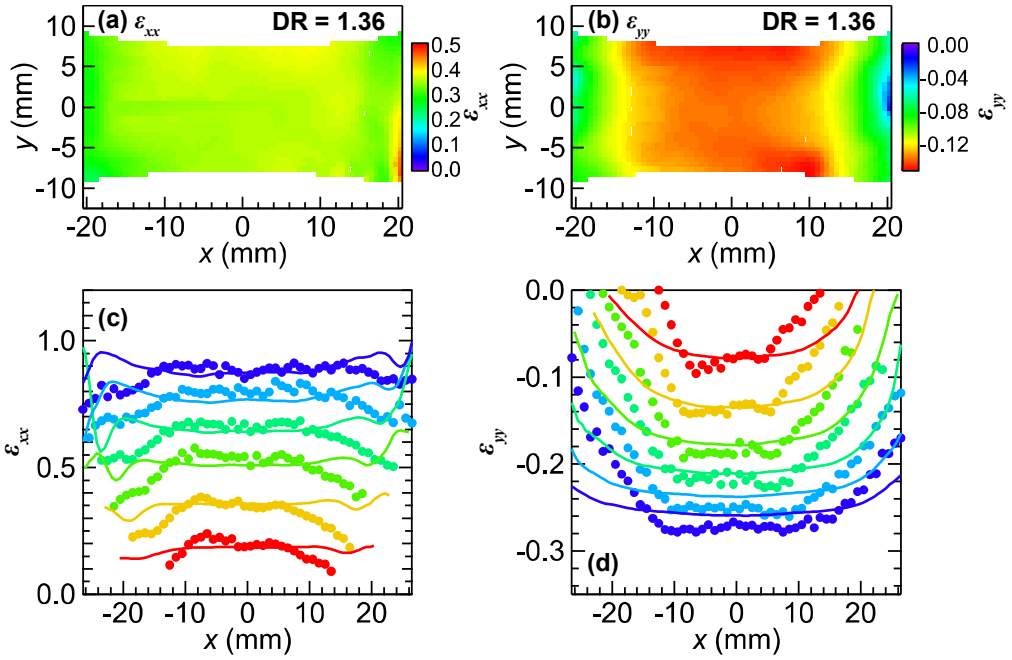

Figure 5.